

# Topological analyses in APP/PS1 mice reveal that astrocytes do not migrate to amyloid- $\beta$ plaques

Elena Galea<sup>a,b,1,2</sup>, Will Morrison<sup>c,1,2</sup>, Eloise Hudry<sup>d</sup>, Michal Arbel-Ornath<sup>d</sup>, Brian J. Bacskai<sup>d</sup>, Teresa Gómez-Isla<sup>d</sup>, H. Eugene Stanley<sup>c,2</sup>, and Bradley T. Hyman<sup>d</sup>

<sup>a</sup>Institució Catalana de Recerca i Estudis Avançats, 08010 Barcelona, Spain; <sup>b</sup>Institut de Neurociències i Unitat de Bioquímica, Facultat de Medicina, Universitat Autònoma de Barcelona, Bellaterra, 08193 Barcelona, Spain; <sup>c</sup>Center for Polymer Studies and Department of Physics, Boston University, Boston, MA 02215; and <sup>d</sup>MassGeneral Institute for Neurodegenerative Disease, Massachusetts General Hospital and Harvard Medical School, Charlestown, MA 02129

Contributed by H. Eugene Stanley, October 23, 2015 (sent for review October 9, 2014; reviewed by Steven E. Arnold and Thomas J. Montine)

**Although the clustering of GFAP immunopositive astrocytes around amyloid- $\beta$  plaques in Alzheimer's disease has led to the widespread assumption that plaques attract astrocytes, recent studies suggest that astrocytes stay put in injury. Here we reexamine astrocyte migration to plaques, using quantitative spatial analysis and computer modeling to investigate the topology of astrocytes in 3D images obtained by two-photon microscopy of living APP/PS1 mice and WT littermates. In WT mice, cortical astrocyte topology fits a model in which a liquid of hard spheres exclude each other in a confined space. Plaques do not disturb this arrangement except at very large plaque loads, but, locally, cause subtle outward shifts of the astrocytes located in three tiers around plaques. These data suggest that astrocytes respond to plaque-induced neuropil injury primarily by changing phenotype, and hence function, rather than location.**

Alzheimer's disease | astrocyte | spatial analysis | sulforhodamine 101 | two-photon

The role of astrocytes in amyloid- $\beta$  deposition during Alzheimer's disease—whether they prevent, potentiate, or have no effect on plaque formation—remains unknown. The peer-reviewed literature indicates that it is widely believed that amyloid- $\beta$  plaques attract astrocytes, with statements such as “astrocytes migrate to amyloid- $\beta$  plaques,” “amyloid- $\beta$  plaques recruit astrocytes,” and variations thereof frequently appearing. The idea that astrocytes are attracted to plaques is an extension of the notion that astrocytes migrate to zones of injury (1, 2) and is mostly based on the immunohistochemical observation that amyloid- $\beta$  deposits are typically surrounded by concentric rings of “reactive astrocytes,” defined by increased GFAP immunoreactivity and hypertrophy. However, recent studies question the capacity of astrocytes to move (3, 4). These suggest instead that astrocytes may be restricted to their birthplace (3), which in the neocortex seems to be within neuronal columns derived from radial glia (5). Recent stereological assessments of astrocytes in Alzheimer's disease suggest that their most prominent change is phenotypic (i.e., GFAP immunoreactivity and hypertrophy) rather than proliferative (6). Thus, doubts have risen over the recruitment of astrocytes by plaques.

Using the APPSwe/PS1dE9 (APP/PS1) double-transgenic mouse model of Alzheimer's disease, we revisited the idea that astrocytes migrate to plaques. Our approach improved on the traditional GFAP immunohistochemical analysis postmortem in three ways. First, the analyses were performed in 3D reconstructions of images captured *in vivo* through cranial windows by two-photon microscopy. These materials are superior to sectioned specimens from fixed brains because they preserve true spatial relationships in 3D to great depths (up to 200  $\mu$ m from the cortical surface), providing accurate positional information for each astrocyte. Second, astrocytes were labeled with sulforhodamine 101 (SR101), a selective fluorescent marker of reactive and nonreactive astrocytes (7), thus avoiding the bias of identifying only a subset of astrocytes as with GFAP. Third, astrocyte and plaque interactions were examined with two mathematical objects: the pair-correlation function  $g(r)$

and the characteristic length ( $L_C$ ) of Voronoi cells. These combine global and plaque-centered perspectives and allow for quantitative comparisons to be made. The  $g(r)$  function was used to assess astrocyte topology, and we examined the effect of plaques on several tiers of astrocytes using  $L_C$ , a very sensitive approach that reveals changes in object position from the redistribution of astrocyte-associated domains approximated by Voronoi tessellation.

Finally, we used simulations to help interpret astrocyte-to-astrocyte and astrocyte-to-plaque interactions and to investigate the effect on astrocyte topology of plaque loads in the upper limit of what could be present in older human patients.

Using a statistical physics approach, we found that astrocytes resemble a liquid of objects of different sizes contained in a constant volume. This arrangement is globally unaltered by plaques except at the heaviest plaque loads.

## Results

### Analysis of Astrocyte Topology Using the Pair-Correlation Function $g(r)$ .

The  $g(r)$  function infers forces between objects distributed in a volume from the patterns in their spatial distribution. Both the range and nature of these interactions can be measured using  $g(r)$ :  $g(r) > 1$  indicates attraction, whereas  $g(r) < 1$  indicates repulsion. At interparticle distances larger than the range of the interaction, the distribution returns to randomness, and  $g(r)$  converges to unity. We measured the pair-correlation function at radius  $R$  by counting the number of objects in a sample space separated by  $R$  and taking the

## Significance

**We sought to identify forces shaping the interaction between astrocytes and amyloid- $\beta$  plaques by performing a spatial analysis, using tools from statistical physics, of 3D images from living transgenic mice. We discovered that astrocytes are repelled by other astrocytes and by plaques. The implications are (i) that a tight balance of repulsive factors maintains the highly territorial astrocyte organization and (ii) that, contrary to a belief widely held by Alzheimer's researchers, astrocytes do not break this order, migrate to plaques, and phagocytose them. We conclude that astrocytes do sense something within the plaque microenvironment, as shown by the dramatic up-regulation of their key molecule, GFAP, but there is little change in position. These small positional changes are directed away from plaques.**

Author contributions: E.G., W.M., E.H., M.A.-O., B.J.B., T.G.-I., H.E.S., and B.T.H. designed research; E.G., W.M., E.H., and M.A.-O. performed research; W.M. contributed new reagents/analytic tools; E.G., W.M., and H.E.S. analyzed data; and E.G., W.M., H.E.S., and B.T.H. wrote the paper.

Reviewers: S.E.A., University of Pennsylvania; and T.J.M., University of Washington.

The authors declare no conflict of interest.

<sup>1</sup>E.G. and W.M. contributed equally to this work.

<sup>2</sup>To whom correspondence may be addressed. Email: hes@bu.edu, Elena.Galea@uab.cat, or wzmorrison@gmail.com.

This article contains supporting information online at [www.pnas.org/lookup/suppl/doi:10.1073/pnas.1516779112/-DCSupplemental](http://www.pnas.org/lookup/suppl/doi:10.1073/pnas.1516779112/-DCSupplemental).

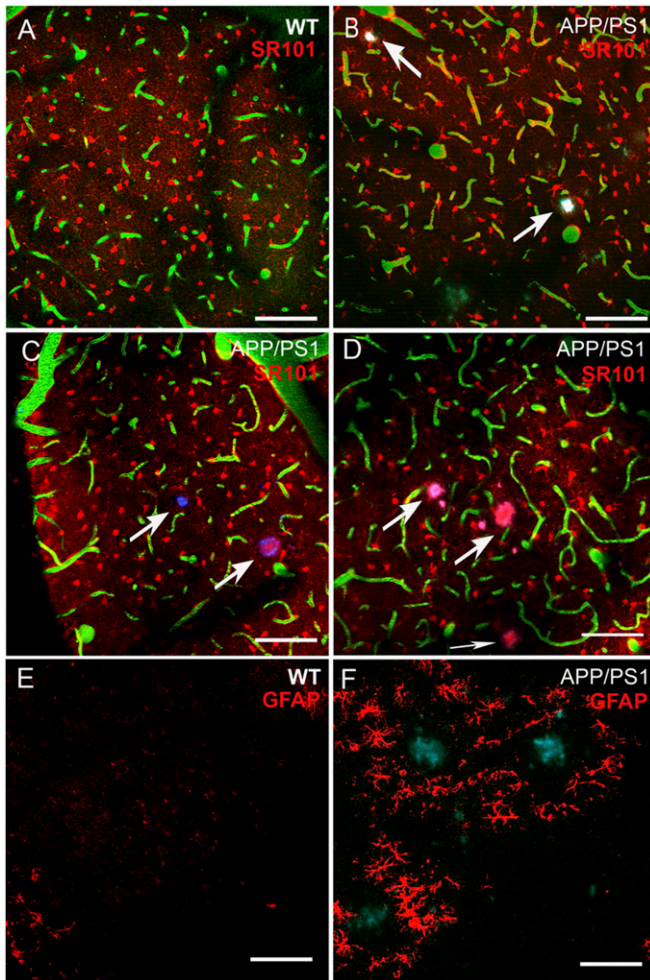


**Fig. 1.** Scattered distribution of astrocytes labeled with SR101. (A–D) Raw multicolor image of astrocytes (red), vessels (green), and plaques (light blue/magenta) in a 6-mo-old WT mouse, and three examples of 9-mo-old APP/PS1 mice. The images are 2D max projections of four planes obtained with ImageJ. Arrows point to plaques. (E and F) GFAP immunohistochemistry in WT and APP/PS1 mice. Here, plaques were stained with thioflavin-S and appear blue-green, and astrocytes are red. Images are max projections of eight stacks of 2  $\mu\text{m}$ . All images span  $0.508 \times 0.508$  mm of cortex. (Scale bars, 80  $\mu\text{m}$ .)

ratio between that number and the number expected for randomly distributed objects in the same sample space at the same density.

We generated the  $g(r)$  function in 5- to 9-mo-old WT and APP/PS1 mice. Transgenic mice have abundant plaque pathology at this age, with plaques representing, in our mice, 0.02–0.205% of the total brain volume imaged at cortical layers 2/3. Additionally, astrocyte density expressed as number of astrocytes per cubic millimeter was  $2.84 \times 10^4 \pm 0.072 \times 10^4$  and  $2.808 \times 10^4 \pm 0.075 \times 10^4$  in WT and APP/PS1 mice, respectively (means  $\pm$  SEM). These data indicate no astrocyte loss in this transgenic model.

As reported (7), topically applied SR101 stained mostly cell bodies and the start of primary processes of astrocytes (Fig. 1A). Astrocytes appeared regularly scattered in both WT and APP/PS1 mice when examined at low magnification (Figs. 1A–D), but visual inspection alone is insufficient to determine whether astrocytes are distributed randomly or are organized in some way [e.g., a lattice, or clusters within columns (5)], or whether plaques have a chemo-attractant effect. Contrary to frequent documentation, and shown here in a brain section from an APP/PS1 mouse stained for GFAP (Fig. 1F), there were no plaque-centered

concentric rings of SR101-positive dots. Fig. 2A and the [Movie S1](#) show a merged image of the individual channels that were separately processed and used for the spatial analyses.

All mice presented a  $g(r)$  function resembling that of a liquid of polydisperse hard spheres. The primary features are a  $g(r) < 1$  region where astrocytes exclude one another in nonoverlapping territories, followed by a transition to  $g(r) > 1$ , and finally a decay to unity. The transition has a finite slope, indicating a finite range of sphere sizes (uniformly sized spheres would show a vertical transition). We parameterized  $g(r)$  by fitting a hyperbolic tangent  $f(x) = \frac{1}{2} + \frac{1}{2} \tanh[(x - X_0)/S]$  with center  $X_0$  and steepness  $S$ . The parameter  $X_0$  measures the minimum allowable separation between the somas of two astrocytes, and  $S$  is proportional to the variability in the minimum separation (Fig. 2D). In WT,  $X_0 = 17.61 \pm 1.25$   $\mu\text{m}$  and  $S = 2.89 \pm 0.57$   $\mu\text{m}$  (means  $\pm$  SEM,  $n = 6$ ). There is a region of enhanced probability of finding a neighbor between 25–50  $\mu\text{m}$ , but the jagged behavior of the function in this zone makes parameterization, and thus any comparison, difficult.

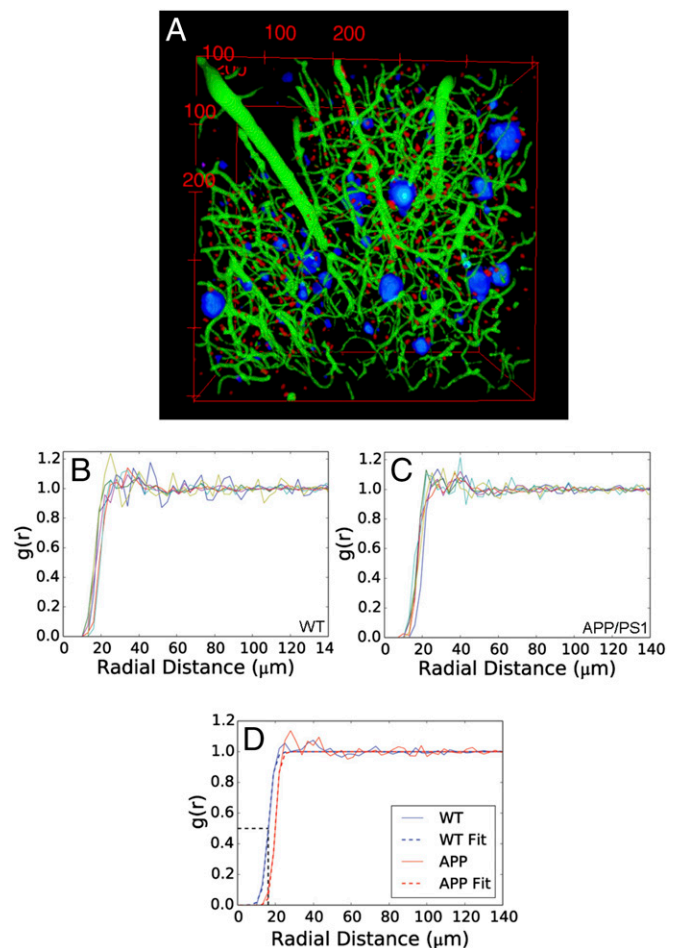


**Fig. 2.** Astrocyte topology fits an exclusion model akin to a hard-sphere liquid. (A) Merging of representative 3D reconstructions of plaques (blue), extracted astrocytes (red), and vessels (green) after processing the raw images. (B and C) Two-point correlations in all mice ( $n = 6$  per genotype). (D) Representative two-point correlations of WT and APP/PS1 mice showing raw data and best fits using  $1/2[1 + \tanh(x - X_0)/S]$ . Astrocytes exclude each other up to 40  $\mu\text{m}$ .  $X_0$ , the distance at which the correlation function reaches 1/2, which is approximately 18  $\mu\text{m}$ , meaning that astrocytes are less than 50% as likely to have a neighbor within 18  $\mu\text{m}$  compared with randomly distributed points. There is no difference between WT and APP/PS1 mice. Average values for  $X_0$  and  $S$  are in the text.

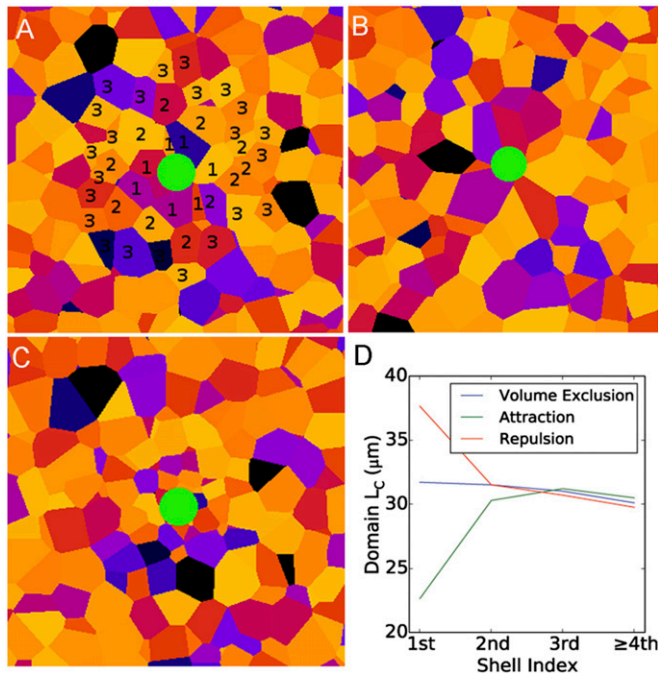


**Fig. 3.** Simulation of the plaque effect on the nearest Voronoi domains. Astrocytes were modeled as thermalized hard-sphere particles in a constant volume. Plaques (in green) were planted in the simulation space. (A) Hard-sphere interactions only. (B and C) Repulsive and attractive interactions, respectively, after simulating the effect of a  $1/r^2$  potential between the plaques and astrocytes. In A tiers around a plaque are numbered 1–3. (D) A plot of domain-size distribution across tiers in three scenarios.

This  $g(r)$  distribution may be related to the well-known non-overlapping astrocyte domains (8). Wilhelmsson et al. (8) observed an average domain diameter of  $43.5 \mu\text{m}$  (within a range of  $36.8$ – $50.9 \mu\text{m}$ ), which roughly coincides with the region of enhanced probability within which the nearest neighbors of an astrocyte are most likely to be found. The minimum exclusion zone of  $17.61 \mu\text{m}$ —which for the sake of simplicity we rounded off to  $18 \mu\text{m}$ —has no obvious anatomical correlate, indicating that there are additional interactions affecting astrocyte positioning.

Adding a foreign body into a liquid of hard spheres contained at a constant volume redistributes the spheres because (i) of “space-occupying” effects and (ii) any attraction or repulsion between the foreign body and the spheres causes the spheres to compete for positions in favorable regions either near to (attraction) or far from (repulsion) the foreign body. This competition increases the interactions among spheres and compresses the astrocyte domains, possibly resulting in a smaller  $S$  and  $X_0$ . If the spheres in favorable regions cannot be compressed to a diameter less than  $X_0$  these parameters will remain unchanged, but the spheres will adopt a close-packed configuration, indicated by a peak in  $g(r)$  at  $X_0$ . However, function, appearance, and parameters for APP/PS1 mice were  $X_0 = 17.51 \pm 1.16 \mu\text{m}$  and  $S = 2.96 \pm 0.46 \mu\text{m}$  (means  $\pm$  SEM,  $n = 6$ ), values not significantly different from those computed in WT mice (Fig. 2 C and D).

Although these results suggest that plaques do not attract astrocytes, because plaques represent a maximum of only 0.205% of brain volume in the mice analyzed, it is possible that only a small subset of astrocytes is affected, or that the magnitude of the interaction at this plaque load compresses domains only slightly. To address these possibilities we increased the sensitivity of the analysis by focusing exclusively on the nearest astrocytes.

**Tiered Analysis of Astrocyte Domain-Volume Distribution Around Plaques.** The Voronoi tessellation subdivides a space containing a set of seed points into multiple regions (cells or domains), such that any point in the domain is closer to the seed of that domain than any other seed. The Voronoi domain is the most finely grained measurement of density possible and is sensitive to details lost in nearest-neighbor-based approaches. Voronoi tessellation has been used to study the spatial arrangement of neurons (9). Here, we used the center of mass of astrocytes as seeds and the characteristic length of a Voronoi domain,  $L_C$ , to compare sizes.

Voronoi domains of astrocyte center-of-masses show two key properties. First, they approximate true astrocyte domains in scenarios such as the “nucleation and growth” examined in ref. 10. This claim is supported by the coincidence between  $L_C$  ( $24.06 \mu\text{m} \pm 0.15$ , means  $\pm$  95% confidence interval) and the astrocyte radius reported in ref. 8. Second, they define geometrical neighbors, thereby allowing analysis of the plaque effect in different tiers of astrocytes (Fig. 3A). This tiered approach is especially advantageous if the effect of a plaque on an astrocyte is “buffered” by other astrocytes, or if the plaque repels the closest astrocytes because of its toxic halo, but still attracts astrocytes at ensuing tiers.

Simulations in which astrocytes were treated as hard spheres revealed that plaques can affect the size of the nearest Voronoi domains. Attraction causes domain size to decrease, and the magnitude of this effect decreases in each tier. Repulsion causes domain size to increase (Fig. 3 A–C). In APP/PS1 mice, the mean domain size is largest in domains bordering the plaque and smaller in each successive tier (Fig. 4A and Table S1). Compared with more distant astrocytes, domain radii in the first, second, and third tiers were enlarged by an average of 4, 2.5, and  $1 \mu\text{m}$ , respectively. Comparison of simulation results to the tier-dependent domain expansion in APP/PS1 mice indicates that plaques push astrocytes away, and that this affects, with diminishing force, at least three tiers of astrocytes.

Finally, to determine whether a subclass of plaques causes the astrocyte shifts, we examined the effect of plaque size on domain expansion in the first tier. Fig. 4C shows a small linear correlation

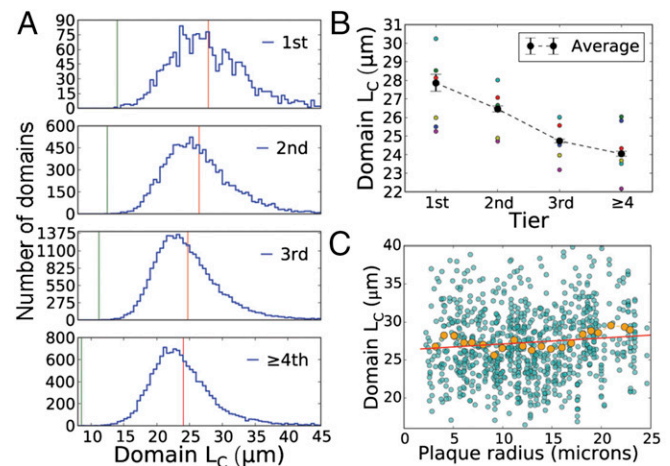


**Fig. 4.** Plaques cause the expansion of the nearest Voronoi domains. The cortical space of APP/PS1 mice was divided among astrocyte seeds by Voronoi tessellation. (A) Distribution of domain radii across shells around plaques in a representative APP/PS1 mouse. The red lines are average radii, and green lines minimum radii. (B) Average change in domain radii showing individual data. Values are the means  $\pm$  95% confidence intervals of six APP/PS1 mice. The number of stacks analyzed per mouse was 4, 10, 8, 13, 16, and 10. Further statistical analysis is provided in Table S1. (C) Scatter plot of plaque sizes and domain radii of the first shell. Data are all domains from all animals combined. Running average is shown in orange and linear fit in red ( $R = 0.098$ ;  $P = 0.0074$ ). Plaque size correlates positively with domain expansion.

between plaque and domain sizes. The average domain radii with respect to plaque radius ( $R$ , micrometers) are  $26.7 \pm 1.0 \mu\text{m}$  for plaques  $R < 3 \mu\text{m}$ ;  $27.0 \pm 0.17 \mu\text{m}$  for plaques  $3 \mu\text{m} < R < 15 \mu\text{m}$ ; and  $28.9 \pm 0.34 \mu\text{m}$  for plaques  $R > 18 \mu\text{m}$ . The values are  $\pm$  SEM of  $n = 6$  mice. The domains near intermediate and large plaques are significantly larger than domains in the control shell ( $P < 0.001$ , using Welch's  $t$  test), and domains near the smallest plaques are not (i.e., the larger the plaque, the more it repels astrocytes).

**Simulation of the Impact of Larger Plaque Loads.** We next investigated whether the small repulsive force detected between astrocytes and plaques, strong enough to cause the nearest astrocytes to move a few microns, would disturb  $g(r)$  at heavier plaque loads. Whereas in APP/PS1 mice the percentage of brain covered by thioflavin or methoxy-labeled plaques can reach 1%, in humans it ranges between 0.8–6.0%, with an average of around 3% (11, 12).

We first increased the plaque load in our simulations with hard-sphere astrocytes to 5% to establish whether plaque load has any impact using a value in the upper limit observed in humans. There is no effect on  $g(r)$  if the only action of the plaque is to occupy space (Fig. 5A and B), but if we introduce a small repulsion between plaques and hard spheres, mimicking the one discovered in the previous analysis, a large peak appears in  $g(r)$  at  $X_0$  (Fig. 5B). This phenomenon occurs because when the plaque load is at 5%, astrocytes attempting to move away from the plaque become more tightly packed, and interastrocyte interaction, particularly the minimum exclusion distance, becomes an important factor. The system also enters a regime in which nearly every astrocyte (>99%) is directly adjacent to a plaque, so that no astrocytes benefit from any buffering of the astrocyte–plaque repulsion by other astrocytes.

We next examined the relationship between plaques and  $g(r)$ , taking into consideration a range of plaque loads and plaque sizes. We found that  $g(r)$  was insensitive to plaque load in the ranges up to 1% (Fig. 5C). The most rapid changes occur between 1 and 3%, with the peak shifting to lower values and transition region steepening. The fraction of astrocytes in the

first tier is a proxy for the percentage strongly affected by plaques. At just less than 1% plaque load, the fraction of first shell domains reaches 50%, and it increases to 90% at a 3% plaque load. The effect is highly dependent on plaque size (Fig. 5D). Although the fraction of astrocytes in the first shell always increases exponentially with plaque load, the change is inversely related to plaque radius, so that small plaques cause a steeper increase. Large plaques concentrate more amyloid in one place, increasing the fraction of volume distant from plaques. At a 3% plaque load, for example—the average in humans—the fraction of astrocytes exposed directly to plaques ranges between 30% and 90% for plaques ranging from 5–20  $\mu\text{m}$ .

In summary, the simulations suggest that, at plaque loads higher than the ones found in transgenic mice, forces maintaining astrocyte topology may be compromised, particularly if small plaques are abundant. This prediction draws attention to the complex, paradoxical impact of plaque size on surrounding astrocytes. Although larger plaques cause larger outward shifts of first-tier astrocytes (Fig. 4C), fewer astrocytes are affected because fewer are in direct contact with plaques (Fig. 5D).

## Discussion

The analysis of astrocyte topology in normal and transgenic mouse brains with methods commonly used in physics has produced two results that may help redefine existing and emerging notions about astrocytes. First, the  $g(r)$  function indicates that the domain-based arrangement of astrocytes is caused by exclusion forces. Second, after mathematically modeling the effect of plaques on such domains, we did not find that plaques attract astrocytes, supporting recent observations suggesting that adult astrocytes do not actively move to sites of injury (3, 4). Although the slight local repulsion caused by plaques seems to have a negligible impact on the global astrocyte topology at low or average plaque loads, the simulations indicate that at the heaviest plaque loads detected in humans the local repulsion may put stress on interastrocyte interactions.

A caveat of the study is that the analysis was cross-sectional and not longitudinal—except with simulations—and that astrocyte recruitment by plaques might have been observed at later times. This notwithstanding, we argue that a procedure sensitive enough to detect a 1- $\mu\text{m}$  outward shift in the third astrocyte tier should have revealed any migration of astrocytes toward plaques if it really occurred. Another caveat is that APP/PS1 mice do not develop tau pathology, or substantial neuronal loss, as seen in brains with Alzheimer's disease. For this reason, a potential additional impact of tau or neuronal death on astrocyte organization or behavior cannot be ruled out.

A key point of the study is the use of SR101 to label astrocytes instead of GFAP immunohistochemistry. Since its discovery as the principal intermediate filament in mature astrocytes in 1969, and the advent of specific immunosera in the early 1970s, GFAP has been the primary marker used to identify astrocytes in basic research and clinical neuropathology. However, because this technique does not stain “nonreactive” astrocytes, we need methods other than GFAP to identify astrocytes and gain a more impartial insight into astrocyte biology. Alternative methods include immunodetection of glutamine synthase or glutamate transporters, which label astrocyte arbors (13), nonspecific body-filling dyes such as GFP and Lucifer yellow (8), and astrocyte-selective markers such as SR101, which is taken up by live astrocytes regardless of the extent of reactivity (7).

SR101-labeled cortical astrocytes were not organized in a high-order pattern (e.g., a lattice) but exhibited  $g(r)$  consistent with organization due to minimal-distance spacing rules. Pair-correlation functions have been widely applied in condensed matter physics (14), cosmology (15), particle engineering (16), and, in the brain, to explore the architecture and connectivity of neurons (17, 18). The overarching goal of these studies was to infer

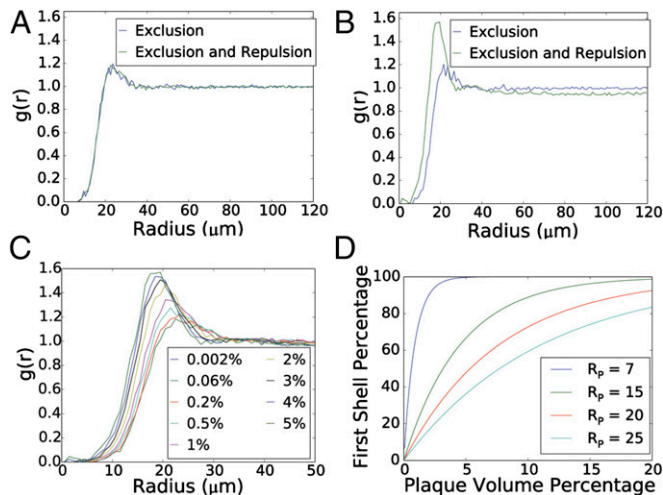


**Fig. 5.** Simulation of the effect of increasing plaque loads on astrocyte topology. (A) No difference in  $g(r)$  at a plaque load of 0.205% even after the addition of a repulsive tension between astrocytes and plaques. (B) At a plaque load of 5%, addition of a repulsive force between astrocytes and plaques forces the impact of the minimum exclusion distance. (C) The  $g(r)$  distortion is directly dependent on plaque load. The most rapid changes occur between 1 and 3%, with the peak shifting to lower values and transition region steepening. (D) The  $g(r)$  distortion is inversely dependent on plaque size. Larger plaques concentrate amyloid in one location, reducing the burden elsewhere.

developmental designs and predict functions from rules governing cell positioning in the adult brain. Neuronal microcolumns have been observed (18), and the possibility that astrocytes are also organized in columns has been investigated in mice. Genetic fate mapping of Cre-labeled precursors in mice has recently revealed the existence of discrete neocortical columns that span from the pial surface to layer 6 and contain both projection neurons and 25- $\mu\text{m}$ -diameter clusters of protoplasmic astrocytes originating from the same radial glia (7). Although in our study some mice showed small peaks at a 25- $\mu\text{m}$  radial distance, the peaks were not sufficiently defined to support astrocyte clustering, perhaps indicating that not all cortical astrocytes originate from radial glia and associate with columns.

Whatever their origin, we found that astrocytes in the adult brain present a minimum exclusion zone of  $\sim 18\ \mu\text{m}$  and a highly probable interneighbor separation of 20–50  $\mu\text{m}$ . Whereas the latter separation is compatible with the range of diameters of astrocyte bodies labeled with Lucifer yellow (8), the minimum exclusion zone has no morphological correlate, which raises the question of its meaning. Following the model used by Pineda et al. (10) to mathematically define the subdivisions of a space after a process of nucleation and growth, we propose that, during development, randomly distributed astrocytes (“seeds”) grow their processes at similar rates until they collide with the processes of other astrocytes and fully occupy cortex. The final position of adult astrocytes is constrained by short-range repulsions from the nearest astrocytes. This scenario suggests that body sizes do not determine adult astrocyte topology, but rather that birthplace and collision forces during development determine the topology and body sizes of adult astrocytes. The nature of such “forces” is unclear, but it is tempting to speculate that, akin to semaphorins and ephrins in neuron-to-neuron interactions, astrocytes produce molecules that repel other astrocytes. If so, the concentration or its gradient may be at a maximum at 18  $\mu\text{m}$ , marking the off-limits zone. All in all, the origin and maintenance of the astrocyte domain-based organization, and its contribution to information processing in cortex, is little understood and a theoretical framework is lacking.

Although the accumulation of amyloid- $\beta$  plaques in 5- to 9-month-old APP/PS1 mice does not perturb the global astrocyte topology, plaques have a local repulsive effect on surrounding astrocytes extending at least three tiers, representing a distance of  $\sim 80\ \mu\text{m}$  from the plaque edge. This effect was deduced from the tiered expansion of astrocyte domains, which simulations indicate reflects an outward shift of the centers-of-mass of astrocytes. Note that because plaque volumes were subtracted from the brain space in our analysis, the space-occupying effect of plaques could cause compression or no change, but never expansion, of astrocyte domains. Note also that the possibility that domain expansion is caused by local astrocyte death, thus leaving more space to other astrocytes, can be ruled out because we detected no difference in global astrocyte density between WT and APP/PS1 mice.

What accounts, then, for the subtle outward shifts of astrocytes? Amyloid- $\beta$  plaques and their microenvironments contain a complex and heterogeneous collection of amyloid- $\beta$  species in different structural conformations and densities. Their impact on pathology is still controversial, and they present different affinities with amyloid-binding dyes. MethoxyO<sub>4</sub>, used in this study, stains only the fibrillar amyloid- $\beta$  in the compact plaque core, but not the halo of soluble oligomeric amyloid- $\beta$  surrounding the core (19). The halo is highly toxic, as shown by the very pronounced loss of excitatory synapses within 6  $\mu\text{m}$  of the plaque edge, coincident with the immunohistochemical detection of soluble oligomeric amyloid- $\beta$  (19). Synapse loss extends up to 50  $\mu\text{m}$  away from the plaque (19), indicating that the halo of soluble oligomeric amyloid- $\beta$  around the plaque is much wider than the volume stained immunohistochemically. Our finding that plaques had an impact over astrocytes within 80  $\mu\text{m}$  of the

plaque edge, mirroring spine loss, can be interpreted in support of a model in which a decreasing gradient of soluble oligomeric amyloid- $\beta$  is toxic to near astrocytes, causing them to try to separate from plaques. Factors released from microglia summoned to the plaque, or damaged neurons, may play a key role, too, in altering astrocyte position. Note that the detection of domain expansion in the second and third tiers disallows a scenario in which astrocyte exclusion from the zone of highest halo toxicity masks any first-tier migration of astrocytes to the plaques.

Our study thus contradicts the widespread belief that plaques and/or their microenvironments act as chemo-attractants for reactive astrocytes. This belief contends that as part of the innate immune defense astrocytes migrate to plaques, phagocytose fibrillar amyloid- $\beta$ , and seal plaque-induced injury with a scar, thereby reducing the growth of plaques and their overall impact. This is based on two pieces of evidence: Astrocytes can migrate to and clear plaques *ex vivo* (20, 21), and impairment of astrocyte activation by deletion of genes encoding for GFAP and vimentin results in increased plaque load in APP/PS1 mice (22). Alternative interpretations of this evidence include the possibilities that (i) *ex vivo* astrocytes come from cultured astrocytes and hence have plastic properties and an ability to migrate that adult astrocytes lack *in situ* (23), and (ii) *gfap* and *vimentin* deletion may abrogate both the capacity of astrocytes to react to injury and also basic functions, for example the clearing of soluble amyloid- $\beta$  by the LDL receptor in an ApoE-dependent manner (24). The increased plaque load in *gfap/vimentin* knockout mice may be hence due to impaired amyloid- $\beta$  clearance rather than to altered phagocytosis. Our study thus changes the view of how astrocytes interact with plaques and presents a model in which astrocytes are passively engaged, if not directly deranged, by plaques or their microenvironments. Should astrocytes limit plaque growth, they do so indirectly by clearing soluble oligomeric amyloid- $\beta$  (24), or by recruiting microglia through the release of soluble chemokines (25, 26).

Our findings are consistent with previous analyses of microglia, astrocyte, and plaque interactions in human brains (6, 27). It was posited that amyloid- $\beta$  attracts microglia but not astrocytes, and that major changes in astrocytes in the vicinity of amyloid- $\beta$  plaques are confined to phenotypic alterations, as revealed by GFAP up-regulation and the development of a “reactive” appearance. To these phenotypic changes we now add the distorted interastrocyte interactions detected in our simulations at heavy plaque loads. The functional alterations associated with these phenomena, and the effect of plaques on astrocyte arbors, remain outstanding questions.

## Materials and Methods

**Animals and Surgery.** APP/PS1 mice were purchased from the Jackson Laboratory (stock number 00462) and bred in-house. These mice express a human mutant amyloid precursor protein gene containing the Swedish mutation K594N/M595L, as well as the presenilin 1 gene deleted for the exon 9, both under the control of the prion promoter (28). Mice were handled according to the guidelines of the Massachusetts General Hospital Institutional Animal Care and Use Committee (IACUC). Mice were 5–9 mo old and of both genders. We used six WT and six APP/PS1 mice. To install cranial windows, mice were anesthetized with 1.5% (vol/vol) isoflurane in oxygen and immobilized in a custom-built stage with mounted ear bars and a nosepiece, similar to a stereotaxic apparatus. A 2- to 3-cm incision was made between the ears, and the scalp was folded back to expose the skull. One circular craniotomy extending to 3–5 mm on both sides of the sagittal suture was performed between Bregma and Lambda using a high-speed drill (Fine Science Tools) and a dissecting microscope (Leica) for gross visualization. Heat and vibration artifacts were minimized during drilling by frequent application of calcium/magnesium PBS (D-PBS; Gibco). The dura was carefully removed with fine forceps. After topical application of SR101, the window was closed with a glass coverslip (8-mm diameter), creating a reservoir filled with D-PBS. The coverslip was sealed to the skull with a mix of dental cement and crazy glue.

**Labeling Procedures.** Methoxy-XO<sub>4</sub> was injected (4 mg/kg *i.p.*) 1 d before each imaging session to label amyloid plaques (29). SR101 (0.25 mg/mL in D-PBS)

was applied topically for 30 min before sealing the craniotomy with a coverslip. Fluorescein-labeled dextran (FITC-dextran, 70,000 Da; Life technologies) was injected into a lateral tail vein (0.2–0.3 mL of 12.5 mg/mL) to visualize vessels.

**In Vivo Imaging.** Images of SR101-labeled astrocytes, amyloid- $\beta$  plaques, and FITC-dextran filled angiograms were obtained by Olympus Fluoview 1000MPE with prechirp optics and a fast AOM mounted on an Olympus BX61WI upright microscope. A wax ring was placed on the edges of the coverslip of the cortical window and filled with distilled water to create a well for an Olympus Optical 25 $\times$  dipping objective (N.A. 1.15). A mode-locked titanium/sapphire laser (Tsunami; Spectra-Physics) generated two-photon fluorescence with an 800-nm excitation, and three photomultiplier tubes (Hamamatsu) collected the emitted light in the range of 380–480, 500–540, and 560–650 nm. Methoxy-XO<sub>4</sub>, FITC-dextran, and SR101 were spectrally separated into these three channels. Stacks of images were collected 0–200  $\mu$ m below the pial surface at a 4- $\mu$ m step and 1 $\times$  zoom. Typically, 5–10 non-overlapping stacks were acquired from each hemisphere.

**Image Processing.** The algorithms used to extract astrocytes, plaques, and vessels are described in [Supporting Information](#) (30–38). Algorithms were implemented through a combination of the Fiji image processing package and custom Python code.

### Spatial Analyses.

**Analysis of astrocyte–astrocyte interaction with the pair-correlation function  $g(r)$ .** The function  $g(r)$  was calculated by first counting the number of pairs of astrocyte centers-of-mass separated by  $d \pm \Delta$ , which we denote  $P_{DD}(d;\Delta)$ . We denote pair counts by  $P$ , with  $D$  subscripts referring to data points, and  $R$  subscripts referring to random points. Several sets of random points (which are equivalent to a noninteracting gas) were generated in the same volume. From these we computed  $P_{RR}(d;\Delta)$ , the number of unique pairs separated by

$d \pm \Delta$  averaged over the sets. The function  $g(r)$  is computed as  $g(r) = P_{DD}(d;\Delta)/P_{RR}(d;\Delta)$ . This formula is the natural estimator of the pair-correlation (see ref. 39 for a comparison of the natural estimator with other estimators). One million random points were generated to compute  $P_{RR}(d;\Delta)$ . The generation of random sets of points is described in detail in [Supporting Information](#). We used an average of 20 random sets of points per stack to compute  $P_{RR}(d;\Delta)$ . Each animal had a minimum of three stacks analyzed, with a mean of 8.6 stacks per animal.

**Plaque-centered analysis by Voronoi tessellation.** Voronoi domains were generated using an algorithm that computes the distance between each pixel and each astrocyte, and pixels were assigned to the Voronoi domain of the nearest astrocyte. Although there exist far more computationally efficient algorithms, this procedure produces Voronoi domains that allow the rough, pixilated, irregularly shaped plaque volumes to be subtracted. The characteristic length of a Voronoi cell was defined as  $L_c = (3Vc/4\pi)^{1/3}$ .

**Computer simulations.** Astrocytes were modeled as hard spheres with a mean diameter of  $X_0$ , and their density was matched to the value of a typical section from an APP/PS1 mouse. Hard spheres representing plaques were added to the simulation space until their volume fraction reached the target range of plaque load. To simulate scenarios in which plaques attract or repel astrocytes, the hard-sphere astrocytes were treated as thermalized particles in a  $1/r^2$  potential (see [Supporting Information](#) and ref. 19).

**ACKNOWLEDGMENTS.** We thank Ksenia Kastanenko and Christopher Williams of the Massachusetts General Hospital for their critical reading of the manuscript. This study was partially funded by Grant PR2011-0511 from the Ministerio de Educación, Cultura y Deporte and Grant BFU2012-38844 from the Ministerio de Economía y Competitividad (to E.G.), a NIH Grants EB000768 and S10 RR025645 (to B.J.B.) and P50 AG005134 (to B.T.H.), and by NIH Grant AG021133 and National Science Foundation Grants CMM1 1125290, PHY-1444389, PHY-0855161, and PHY-1505000 (to W.M. and H.E.S.).

- Pekny M, Nilsson M (2005) Astrocyte activation and reactive gliosis. *Glia* 50(4):427–434.
- Sofroniew MV (2009) Molecular dissection of reactive astrogliosis and glial scar formation. *Trends Neurosci* 32(12):638–647.
- Tsai HH, et al. (2012) Regional astrocyte allocation regulates CNS synaptogenesis and repair. *Science* 337(6092):358–362.
- Bardehle S, et al. (2013) Live imaging of astrocyte responses to acute injury reveals selective juxtavascular proliferation. *Nat Neurosci* 16(5):580–586.
- Magavi S, Friedmann D, Banks G, Stolfi A, Lois C (2012) Coincident generation of pyramidal neurons and protoplasmic astrocytes in neocortical columns. *J Neurosci* 32(14):4762–4772.
- Serrano-Pozo A, Gómez-Isla T, Growdon JH, Froesch MP, Hyman BT (2013) A phenotypic change but not proliferation underlies glial responses in Alzheimer disease. *Am J Pathol* 182(6):2332–2344.
- Nimmerjahn A, Kirchhoff F, Kerr JN, Helmchen F (2004) Sulforhodamine 101 as a specific marker of astroglia in the neocortex in vivo. *Nat Methods* 1(1):31–37.
- Wilhelmsson U, et al. (2006) Redefining the concept of reactive astrocytes as cells that remain within their unique domains upon reaction to injury. *Proc Natl Acad Sci USA* 103(46):17513–17518.
- Duyckaerts C, Godefroy G (2000) Voronoi tessellation to study the numerical density and the spatial distribution of neurones. *J Chem Neuroanat* 20(1):83–92.
- Pineda E, Garrido V, Crespo D (2007) Domain-size distribution in a Poisson-Voronoi nucleation and growth transformation. *Phys Rev E Stat Nonlin Soft Matter Phys* 75(4 Pt 1):040107.
- Urbanc B, et al. (2002) Neurotoxic effects of thioflavin S-positive amyloid deposits in transgenic mice and Alzheimer's disease. *Proc Natl Acad Sci USA* 99(22):13990–13995.
- Perez-Nievas BG, et al. (2013) Dissecting phenotypic traits linked to human resilience to Alzheimer's pathology. *Brain* 136(Pt 8):2510–2526.
- Kulijewicz-Nawrot M, Syková E, Chvátal A, Verkhratsky A, Rodriguez JJ (2013) Astrocytes and glutamate homeostasis in Alzheimer's disease: A decrease in glutamine synthetase, but not in glutamate transporter-1, in the prefrontal cortex. *ASN Neuro* 5(4):273–282.
- Rahman A (1964) Correlations in the motion of atoms in liquid argon. *Phys Rev* 136: A405.
- Davis M, Peebles PJE (1983) A survey of galaxy redshifts. V-The two-point position and velocity correlations. *Astrophys J* 267:465–482.
- Zhang Z, Keys AS, Chen T, Glotzer SC (2005) Self-assembly of patchy particles into diamond structures through molecular mimicry. *Langmuir* 21(25):11547–11551.
- Eglen SJ, Lofgreen DD, Raven MA, Reese BE (2008) Analysis of spatial relationships in three dimensions: Tools for the study of nerve cell patterning. *BMC Neurosci* 9:68.
- Buldyrev SV, et al. (2000) Description of microcolumnar ensembles in association cortex and their disruption in Alzheimer and Lewy body dementias. *Proc Natl Acad Sci USA* 97(10):5039–5043.
- Koffie RM, et al. (2009) Oligomeric amyloid beta associates with postsynaptic densities and correlates with excitatory synapse loss near senile plaques. *Proc Natl Acad Sci USA* 106(10):4012–4017.
- Wyss-Coray T, et al. (2003) Adult mouse astrocytes degrade amyloid-beta in vitro and in situ. *Nat Med* 9(4):453–457.
- Koistinaho M, et al. (2004) Apolipoprotein E promotes astrocyte colocalization and degradation of deposited amyloid-beta peptides. *Nat Med* 10(7):719–726.
- Kraft AW, et al. (2013) Attenuating astrocyte activation accelerates plaque pathogenesis in APP/PS1 mice. *FASEB J* 27(1):187–198.
- Lichtenstein MP, Madrigal JL, Pujol A, Galea E (2012) JNK/ERK/FAK mediate promigratory actions of basic fibroblast growth factor in astrocytes via CCL2 and COX2. *Neurosignals* 20(2):86–102.
- Vergheze PB, et al. (2013) ApoE influences amyloid- $\beta$  (A $\beta$ ) clearance despite minimal apoE/A $\beta$  association in physiological conditions. *Proc Natl Acad Sci USA* 110(19): E1807–E1816.
- El Khoury J, et al. (2007) Ccr2 deficiency impairs microglial accumulation and accelerates progression of Alzheimer-like disease. *Nat Med* 13(4):432–438.
- Meyer-Luehmann M, et al. (2008) Rapid appearance and local toxicity of amyloid-beta plaques in a mouse model of Alzheimer's disease. *Nature* 451(7179):720–724.
- Serrano-Pozo A, et al. (2013) Differential relationships of reactive astrocytes and microglia to fibrillar amyloid deposits in Alzheimer disease. *J Neuropathol Exp Neurol* 72(6):462–471.
- Jankowsky JL, et al. (2001) Co-expression of multiple transgenes in mouse CNS: A comparison of strategies. *Biomol Eng* 17(6):157–165.
- Klunk WE, et al. (2002) Imaging A $\beta$  plaques in living transgenic mice with multiphoton microscopy and methoxy-XO<sub>4</sub>, a systemically administered Congo red derivative. *J Neuropathol Exp Neurol* 61(9):797–805.
- Castle M, Keller J (2007) Rolling ball background subtraction. Available at [rsb.info.nih.gov/ij/plugins/rolling-ball.html](http://rsb.info.nih.gov/ij/plugins/rolling-ball.html).
- Bernsen J (1986) Dynamic thresholding of grey-level images. *Proceedings of the 8th International Conference on Pattern Recognition*, eds Burduk R, Jackowski K, Kurzynski M, Wozniak M, Zolnierok A (Springer, New York), pp 1251–1255.
- Landini G (2011) Auto threshold and auto local threshold. Available at [fiji.sc/Auto\\_Local\\_Threshold](http://fiji.sc/Auto_Local_Threshold).
- Otsu N (1979) A threshold selection method from gray-level histograms. *IEEE Trans Syst Man Cybern* 9:62–66.
- Kapur JN, Sahoo PK, Wong ACK (1985) A new method for gray-level picture thresholding using the entropy of the histogram. *Graph Models Image Proc* 29(3):273–285.
- Longair M (2013) Find Connected Regions. Available at [www.longair.net/edinburgh/imagej/find-connected-regions](http://www.longair.net/edinburgh/imagej/find-connected-regions).
- Prewitt JMS, Mendelsohn ML (1966) The analysis of cell images. *Ann N Y Acad Sci* 128(3):1035–1053.
- Ollion J, Cochenne J, Loll F, Escudé C, Boudier T (2013) TANGO: A generic tool for high-throughput 3D image analysis for studying nuclear organization. *Bioinformatics* 29(14):1840–1841.
- Bolte S, Cordelières FP (2006) A guided tour into subcellular colocalization analysis in light microscopy. *J Microsc* 224(Pt 3):213–232.
- Kerscher M, Szapudi I, Szalay AS (2000) A comparison of estimators for the two-point correlation function. *Astrophys J Lett* 535:1:L13.